High electrical conductivity and high porosity in a Guest@MOF material: evidence of TCNQ ordering within Cu_3BTC_2 micropores

Christian Schneider[a], Dardan Ukaj[a], Raimund Koerver[b], A. Alec Talin[c], Gregor Kieslich[a], Sidharam P. Pujari[d], Han Zuilhof[d,e], Jürgen Janek[b], Mark D. Allendorf[*c], Roland A. Fischer[*a]

a Department of Chemistry, Technical University Munich, Lichtenbergstrasse 4, D-85748 Garching, Germany
b Institute of Physical Chemistry & Center for Materials Research (ZFM), Justus-Liebig-University Giessen, Heinrich-Buff-Ring 17, 35392 Giessen, Germany
c Sandia National Laboratories, Livermore, CA 94551, USA
d Laboratory of Organic Chemistry, Wageningen University & Research, Stippeneng 4, 6708 WE Wageningen, The Netherlands
e School of Pharmaceutical Sciences and Technology, Tianjin University, 92 Weijin Road, Tianjin, P.R. China

Contents

Powder X-ray diffraction (PXRD)

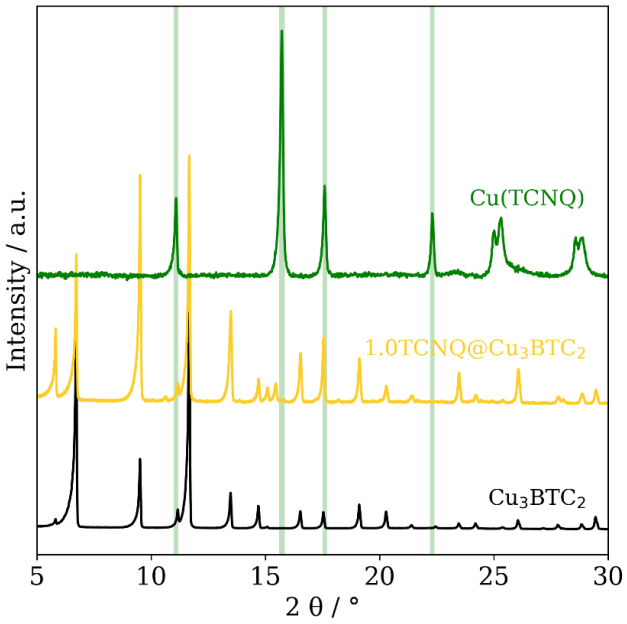

Figure S 1: Powder X-ray diffraction (PXRD) pattern of pristine Cu_3BTC_2 (black), 1.0TCNQ@Cu_3BTC_2 and Cu(TCNQ) prepared following the literature procedure.[1] Vertical lines indicate the reflection positions of Cu(TCNQ). The principal reflection of Cu(TCNQ) can be found in the diffraction pattern of 1.0TCNQ@Cu_3BTC_2.

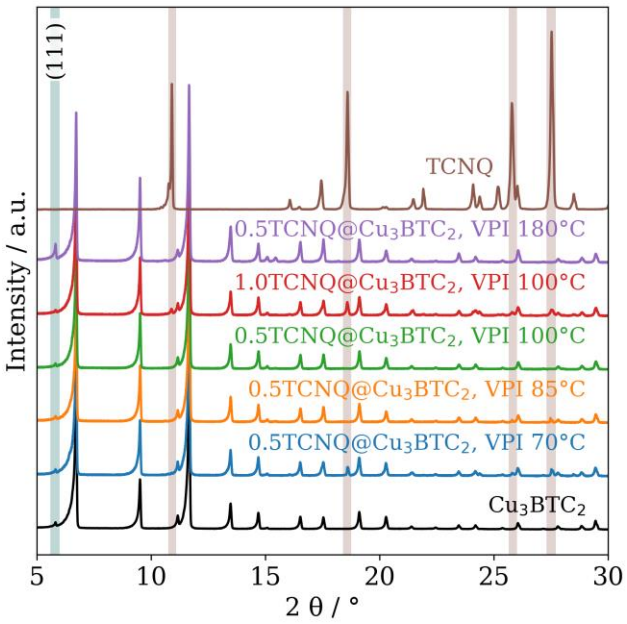

Figure S 2: PXRD pattern of pristine Cu_3BTC_2 (black), Cu_3BTC_2 loaded with TCNQ at different reaction temperatures and TCNQ (brown). The pronounced (111) reflection is absent for samples infiltrated at low temperatures. Instead, new reflections attributed to unreacted TCNQ become apparent.

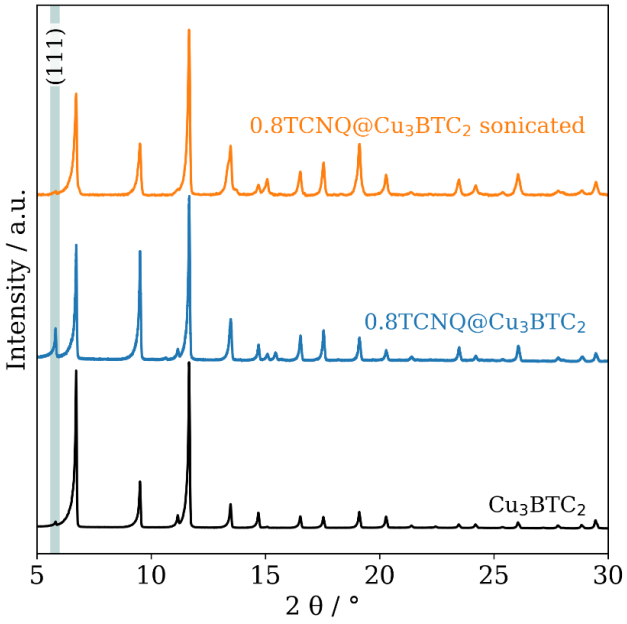

Figure S 3: Powder X-ray diffraction (PXRD) pattern of pristine Cu_3BTC_2 (black), 0.8TCNQ@Cu_3BTC_2 before (blue) and after sonication in hexane (orange). The crystal structure of the MOF remains intact after sonication, but the intensity of the (111) reflection and additional reflections attributed to a systematic arrangement of TCNQ vanish.

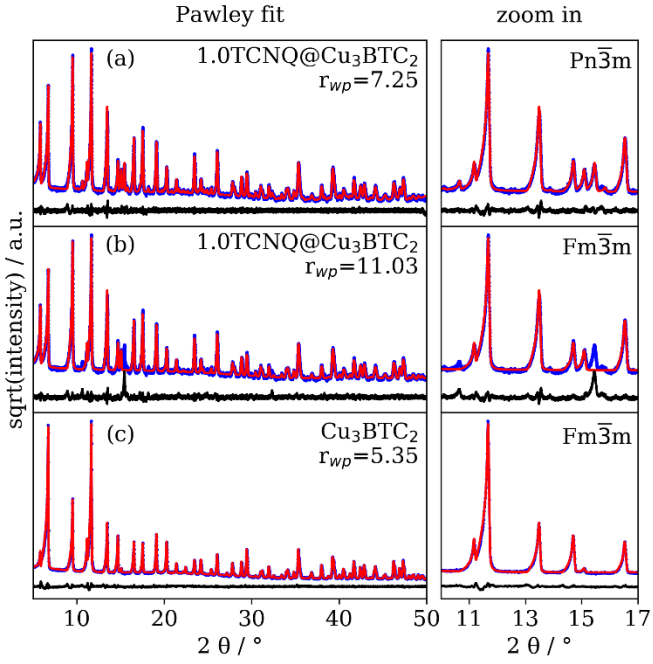

Figure S 4: Pawley profile fit 1.0TCNQ@Cu_3BTC_2 using the space group Pn-3m (a) and Fm-3m (b) and of Cu_3BTC_2 (c). The experimental data, profile fit and their difference are plotted in blue, red, and black, respectively. The weighted profile R-factor (r_{WP}) for each fit is shown in each diagram. A zoom in is shown on the right-hand side. Although the diffraction pattern of Cu_3BTC_2 can be fitted in the space group Fm-3m, not all reflections of 1.0TCNQ@Cu_3BTC_2 can be indexed using the same space group. A profile fit using the primitive space group Pn-3m, however, can account for all new reflections.

Theoretical BET surface area if TCNQ does not penetrate the MOF

The accessible pore volume of the MOF would remain unchanged in a physical mixture of Cu_3BTC_2 and TCNQ if TCNQ was not capable of diffusing into the MOF pores during the VPI process. Consequently, during a porosimetry measurement, only the additional mass of the non-porous TCNQ would contribute to the decrease of the BET surface area compared to the pristine MOF. The measured BET surface area of pristine Cu_3BTC_2 (BTC = 1,3,5-benzenetricarboxylate) amounts to 1833.0 m^2/g. For a sample with the composition n(TCNQ) / n(Cu_3BTC_2) = 1, denoted as 1.0TCNQ@Cu_3BTC_2, the relative weight percentage of TCNQ amounts to 25.2%. In case of a physical mixture, the presence of TCNQ would result in a loss in BET surface area of 463.6 m^2/g to 1370.4 m^2/g. The prepared sample 1.0TCNQ@Cu_3BTC_2, however, has a BET surface area of only 574 m^2/g, which is clear evidence for the incorporation of TCNQ in Cu_3BTC_2.

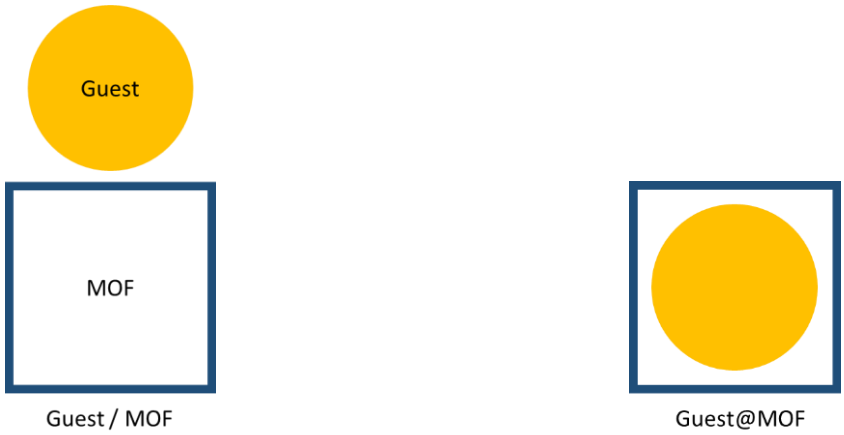

Figure S 5: Schematic illustration of the difference between a physical mixture of a MOF plus a guest material (left) and a Guest@MOF material (right) to illustrate the implication of the two scenarios on the BET surface area.

Infrared (IR) spectroscopy

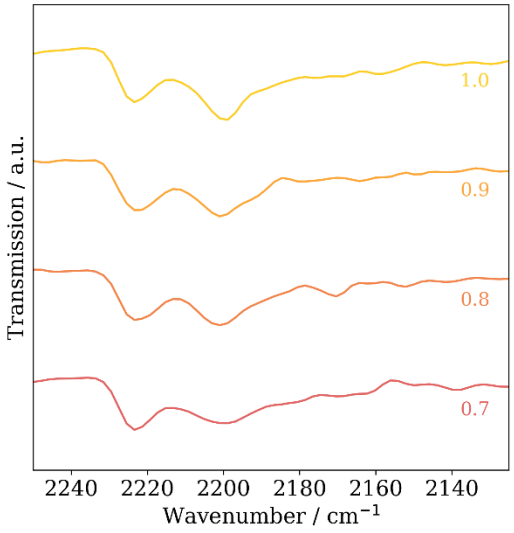

Figure S 6: IR spectra in the CN vibration region of *x*TCNQ@Cu_3BTC_2 with high loadings (value for *x* indicated below spectrum).

Thermogravimetric analysis (TGA) and differential scanning calorimetry (DSC)

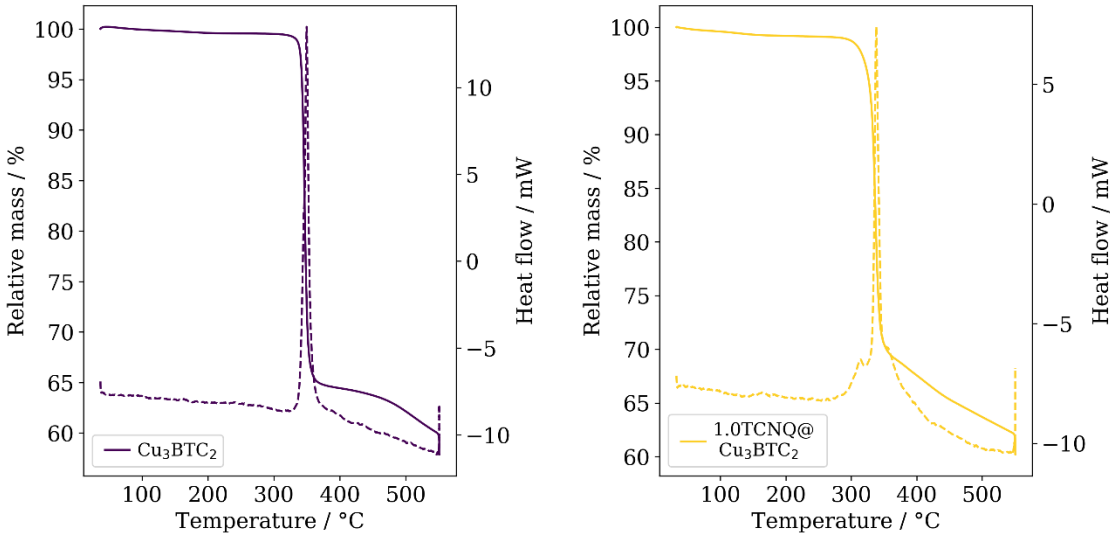

Figure S 7: TGA (solid line) and DSC (dashed line) of pristine Cu_3BTC_2 (left) and 1.0TCNQ@Cu_3BTC_2 (right).

Electrical conductivity measurements

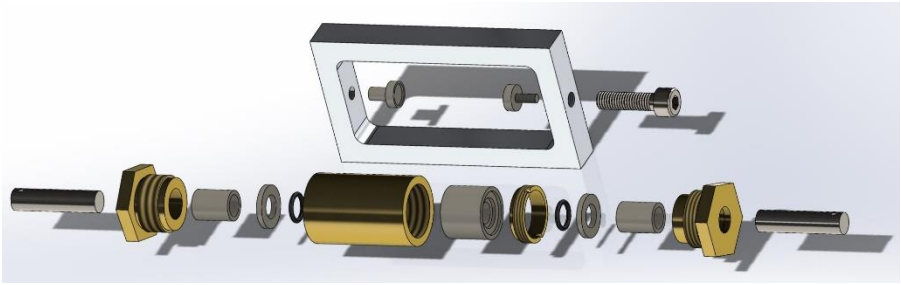

Figure S 8: Schematic of the air-tight press cell used for electrical conductivity measurements. MOF powder is filled into the assembled cell compressed between the two outer stainless steel pistons. PEEK elements serve as electrical insulation from the brass parts. After the powder is pressed to a pellet, the cell is mounted into an aluminum frame and fixed with a screw applying a torque of 10 Nm to maintain pressure on the pressed pellet. The stainless steel cylinders serve as electrodes for the conductivity measurements.

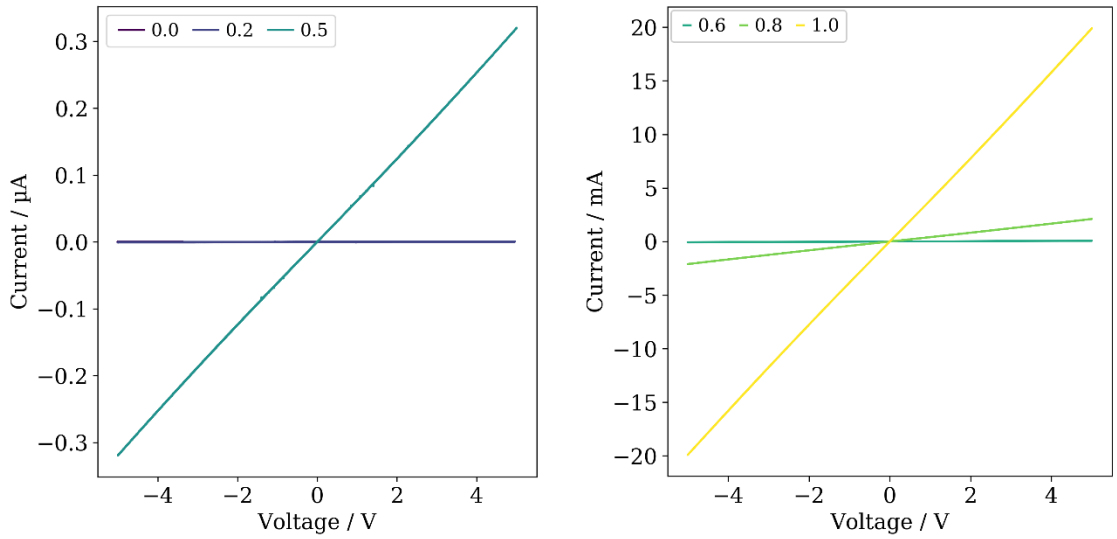

Figure S 9: *IV*-curves of TCNQ-loaded Cu_3BTC_2 samples. Figure divided into two plots for clarity (different scale of y-axis).

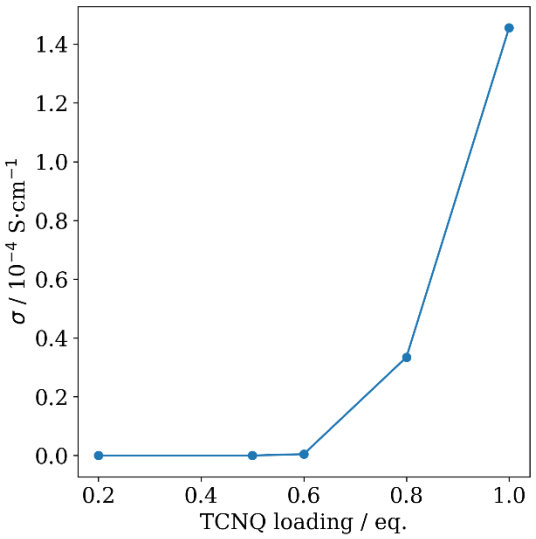

Figure S 10: Calculated conductivities of TCNQ-loaded Cu_3BTC_2 samples plotted versus loading amount.

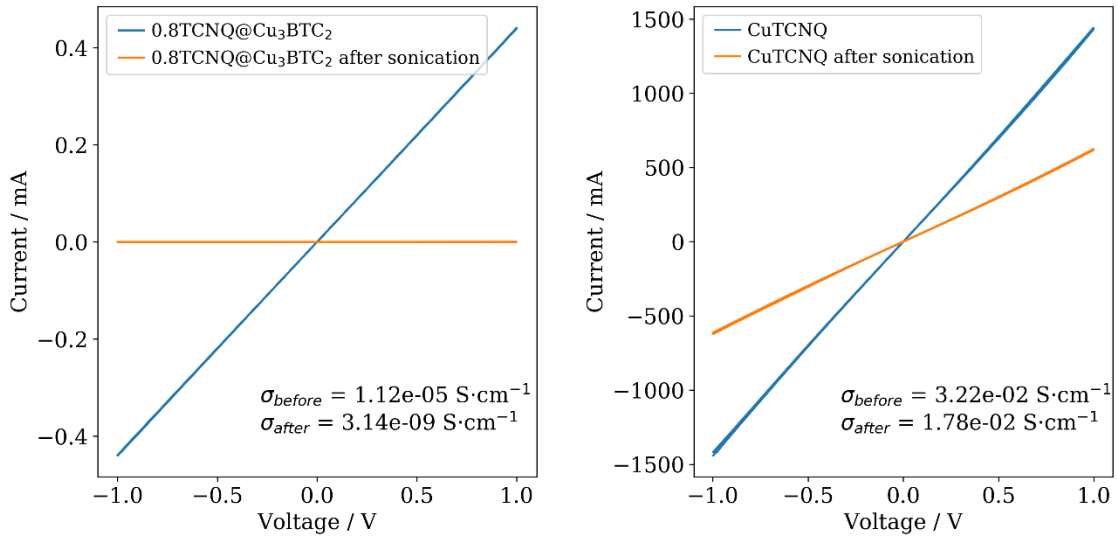

Figure S 11: *IV*-curves of 0.8TCNQ@Cu3BTC2 and pristine Cu(TCNQ) before and after 1 hour sonication in hexane. Conductivity of 0.8TCNQ@Cu3BTC2 drops by four orders of magnitude while the conductivity of pristine Cu(TCNQ) shows only small changes.

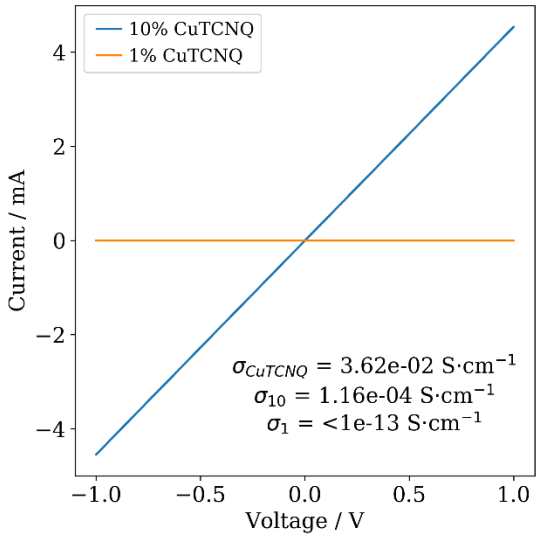

Figure S 12: *IV* curves of pressed pellets of physical mixtures of 1% and 10% CuTCNQ mixed with pristine Cu_3BTC_2. Conductivities of both mixtures and of pristine CuTCNQ are given in the diagram.

Table S 1: Pellet thicknesses for the calculation of the conductivity.

Sample	pellet thickness / mm
Cu_3BTC_2	0.30
0.2TCNQ@ Cu_3BTC_2	0.37
0.5TCNQ@ Cu_3BTC_2	0.47
0.6TCNQ@ Cu_3BTC_2	0.28
0.8TCNQ@ Cu_3BTC_2	0.63
1.0TCNQ@ Cu_3BTC_2	0.29
Cu(TCNQ)	0.18
0.8TCNQ@ Cu_3BTC_2 (sonnication)	0.20
Cu(TCNQ) (sonnication)	0.18
CuTCNQ/ Cu_3BTC_2 99:1	0.053
CuTCNQ/ Cu_3BTC_2 9:1	0.043

Auger electron spectroscopy (AES)

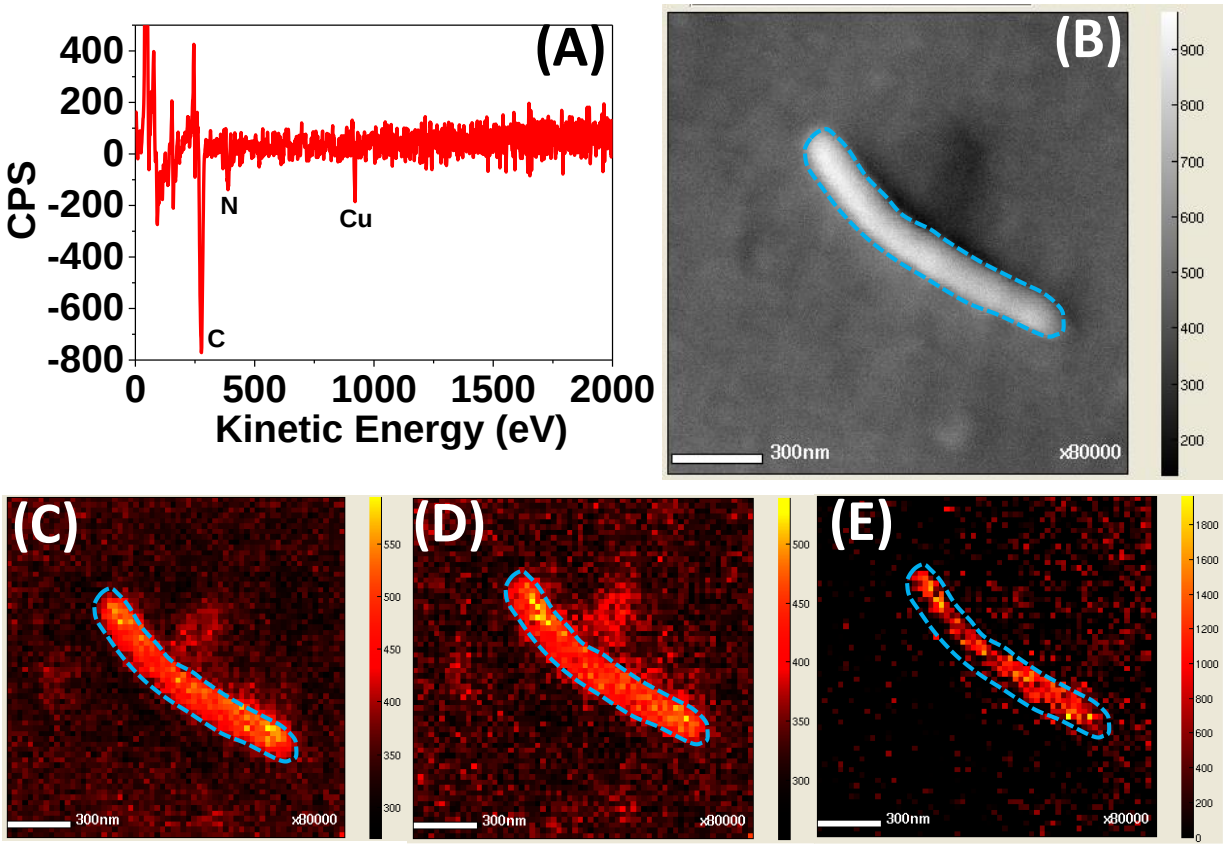

Figure S 13: AES spectra (A), SEM image (B) and AES image of a Cu(TCNQ) nano-wire that has formed on the surface of a Cu_3BTC_2.crystal during the VPI process. Bottom images showing a homogeneous distribution of C (C), N (D), and Cu (E).

Scanning electron microscopy (SEM) images

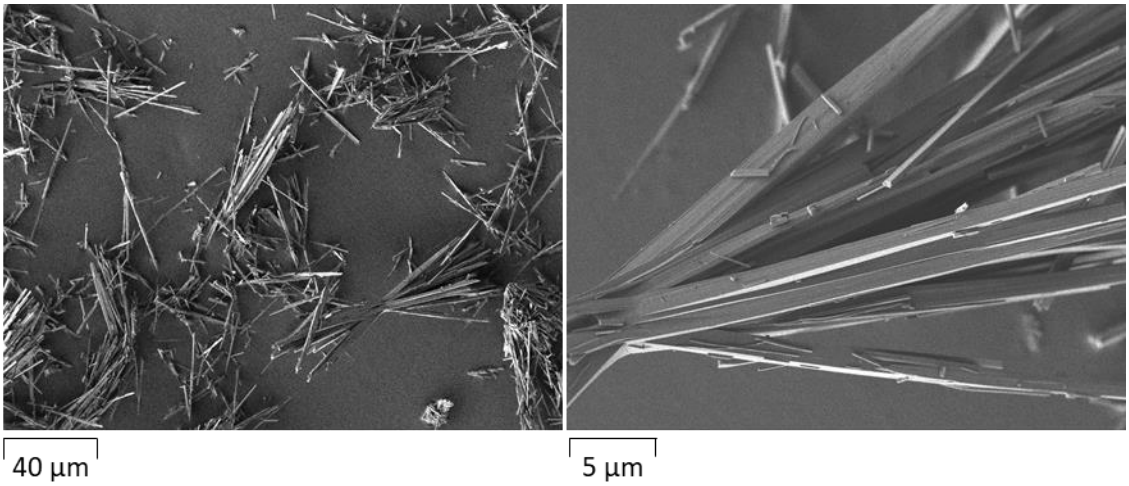

Figure S 14: SEM images of needle-shaped Cu(TCNQ) crystals prepared following the literature procedure.[1]

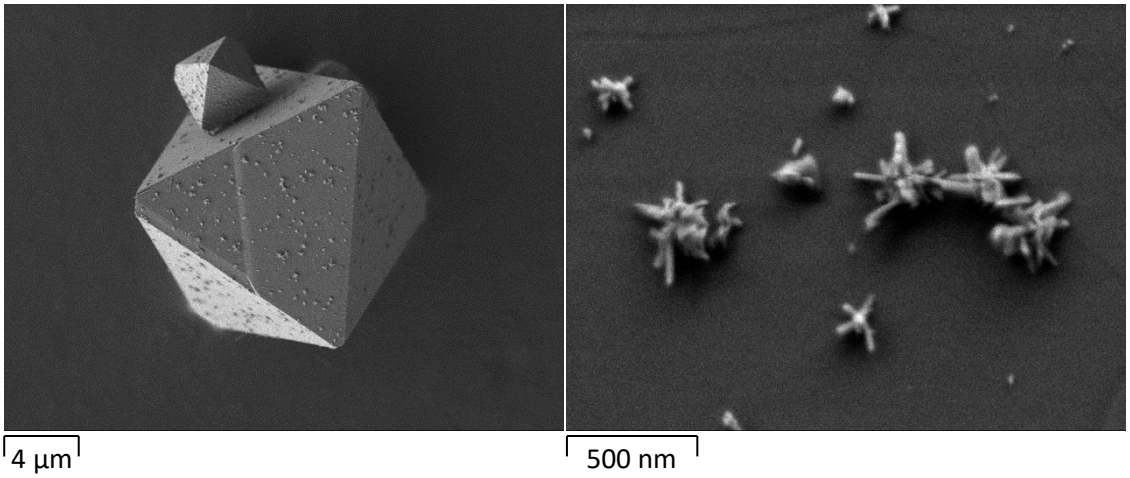

Figure S 15: SEM images of 0.5 TCNQ@Cu_3BTC_2 synthesized at 100 °C.

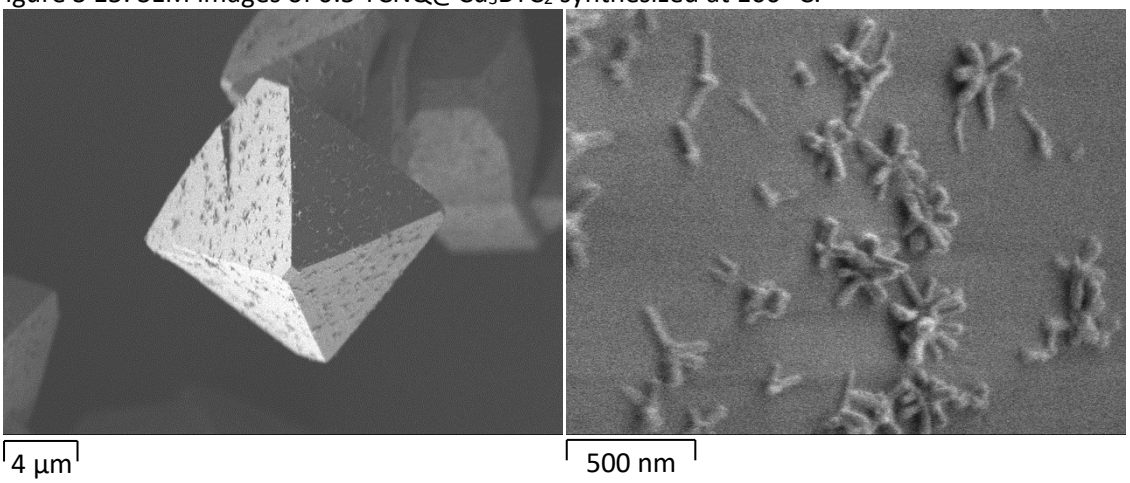

Figure S 16: SEM images of 1.0 TCNQ@Cu_3BTC_2 synthesized at 100 °C.

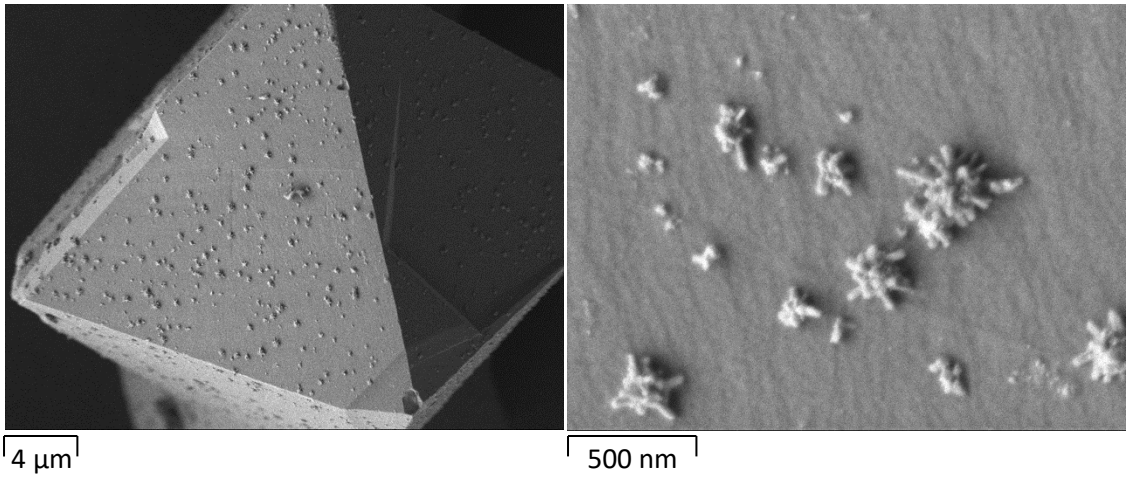

Figure S 17**:** SEM images of 0.5 TCNQ@Cu_3BTC_2 synthesized at 70 °C. To overcome the low vapor pressure of TCNQ at these low temperatures, the synthesis was performed in high-vacuum flame sealed glass ampoules at a pressure of 10^{-5} mbar.

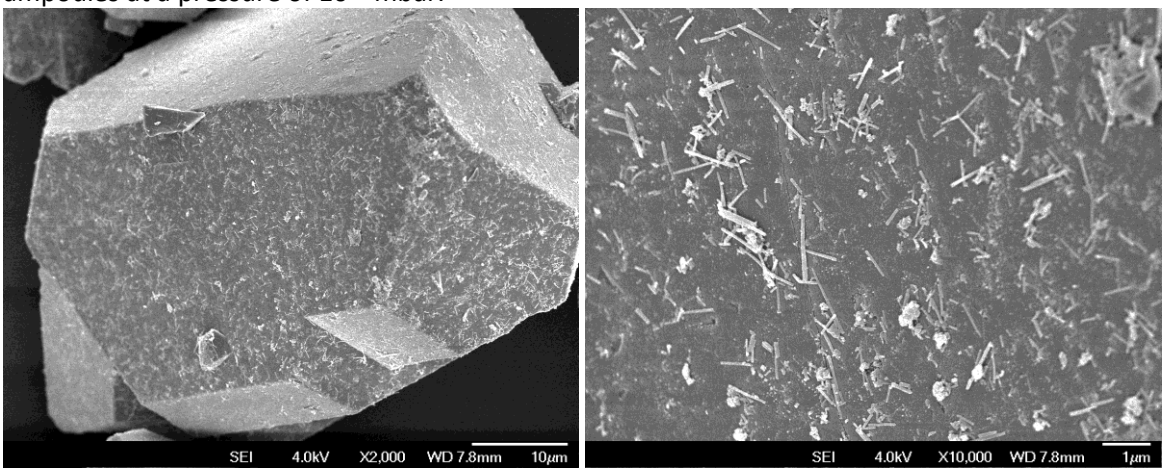

Figure S 18: SEM images of 0.8 TCNQ@Cu_3BTC_2 synthesized at 180 °C after sonication in hexane for 1 hour.

X-ray photoelectron spectroscopy (XPS)

We acknowledge the constructive referee comments which have motivated us do a thorough analysis of the XPS data. XPS is a highly surface sensitive method that is used to probe the binding energy and thus the oxidation state of Cu and N present in the sample. It has to be noted, that this technique does not provide localized information but rather an average over the sample.

The Cu $2p_{3/2}$ regime of the XPS spectra of Cu_3BTC_2 (a) and samples loaded with 0.5 (b) and 1.0 equivalents of TCNQ (c) are shown in Figure S 19. Integration of the Cu(I) and Cu(II) peak fits reveals Cu(I)/Cu(II) ratios of 1.50, 2.62, and 2.36, respectively. From the literature,[2-3] we know that thermal activation (vacuum, elevated temperatures) causes reduction of Cu(II) species in Cu_3BTC_2. Cu(I) species are likely to form at the surface of the crystallites due to an incomplete coordination shell and according charge compensation of the exposed Cu ions. This explains the high Cu(I)/Cu(II) ratio at the surface of pristine Cu_3BTC_2. The prolonged thermal treatment during the VPI process (3 days at 180 °C) causes the formation of further Cu(I) species and hence higher Cu(I)/Cu(II) ratios for the infiltrated samples. The amount of Cu(I) formed during the treatment is assumed to be the same for all samples and independent of the amount of TCNQ used in the VPI reaction. However, TCNQ is a good electron acceptor and can thus serve as an oxidizing agent. As a result, neutral TCNQ can oxidize Cu(I) species back to Cu(II) giving rise to the formation of CuTCNQ at the surface of the crystallites ($2\ Cu^{I} + TCNQ^{0} \rightarrow Cu^{II} + Cu^{I}TCNQ^{-I}$). From SEM data we see that this reaction occurs increasingly with increasing amount of TCNQ provided in the synthesis. Consequently, a decreasing Cu(I)/Cu(II) ratio is expected for samples with higher TCNQ loading, which is exactly what we see comparing the results for 0.5TCNQ@Cu_3BTC_2 and 1.0TCNQ@Cu_3BTC_2. It is important to note, that XPS detects Cu(I) species from both Cu(TCNQ) and surface defects of the MOF. Therefore, the amount of CuTCNQ nanowires seen in SEM images cannot be directly correlated with the amount of Cu(I) found by analysis of the XPS data.

The XPS signature in the N1s regime for TCNQ matches well with the literature reference,[4] and changes upon infiltration with TCNQ (Figure S 20). While the spectra of TCNQ could be easily fitted by two Gauss-Lorentz peak shapes, the spectra for 0.5TCNQ@Cu_3BTC_2 and 1.0TCNQ@Cu_3BTC_2 are more complex. The most plausible fit could be achieved using two peaks that, however, show a significant broadening compared to the fits for pristine TCNQ. Moreover, the position of the green peak is shifted to slightly lower binding energies. As the XPS spectra represent the chemical environment at the surface of the particles, significant contributions of the TCNQ radical anion of CuTCNQ can be assumed. Moreover, coordinated and uncoordinated nitrile groups of TCNQ molecules (ordered and disordered) will give a different signal. Therefore, we believe that the peak at higher binding energies, which was assigned as a shake-up in the spectrum of TCNQ,[4] here consists of contributions from the different TCNQ species, which account for the significant broadening of the fitted peaks.

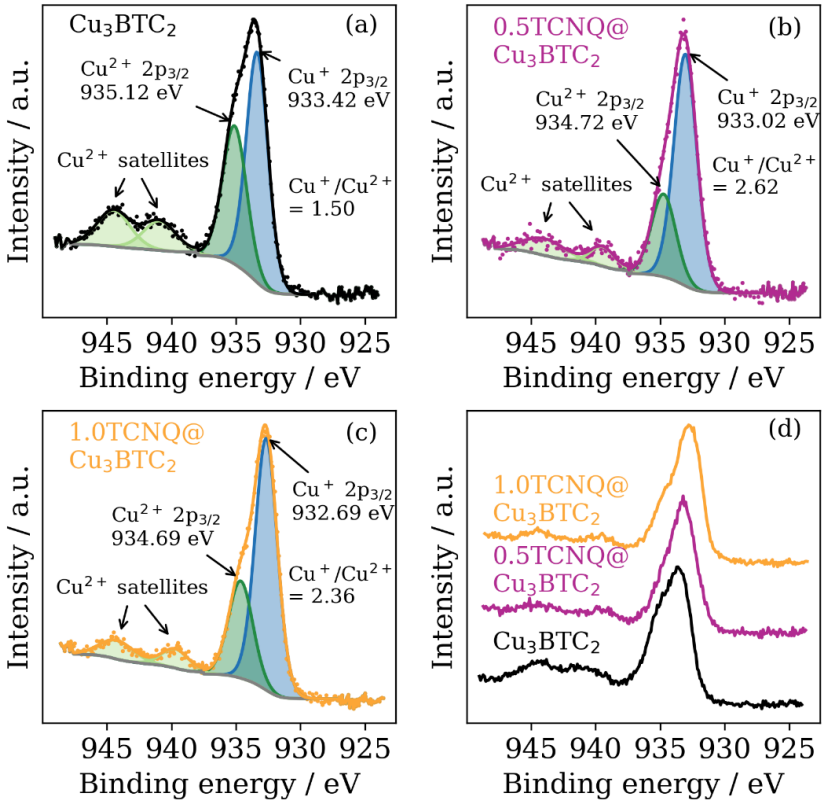

Figure S 19: XPS analysis of the Cu 2p region of Cu_3BTC_2 (a), 0.5 TCNQ@Cu_3BTC_2 (b), and 1.0 TCNQ@Cu_3BTC_2 (c) and a comparison plot of the normalized spectra (d). Cu(I)/Cu(II) ratios based on the peak integrals are given in the diagram.

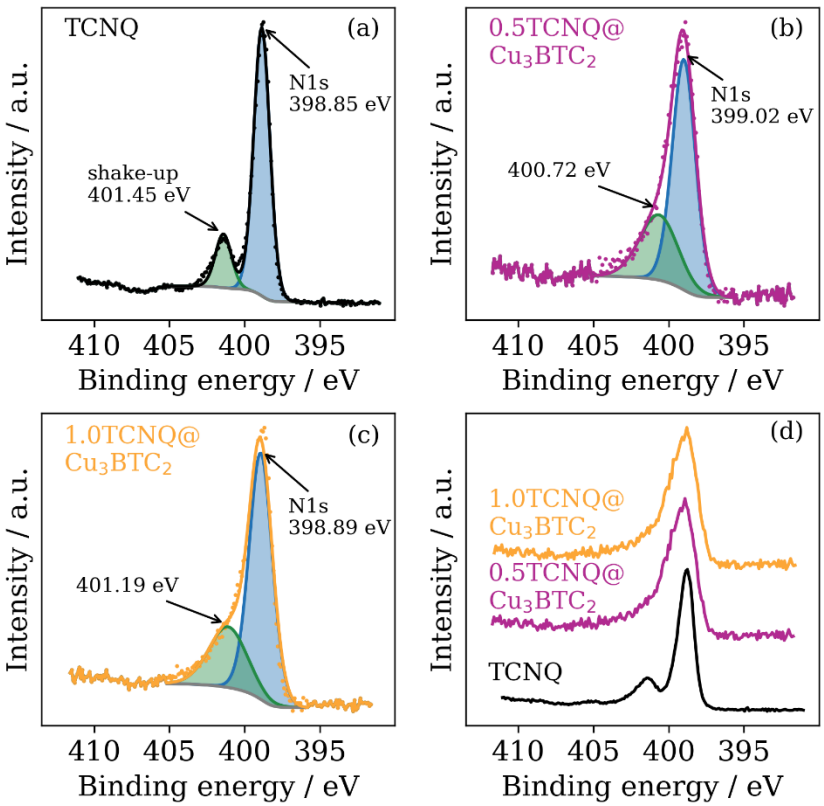

Figure S 20: XPS analysis of the N 1s region of Cu_3BTC_2 (a), 0.5 TCNQ@Cu_3BTC_2 (b), and 1.0 TCNQ@Cu_3BTC_2 (c) and a comparison plot of the normalized spectra (d).

Elemental analysis

Table S 2 Elemental analysis of the concentration series of TCNQ@Cu_3BTC_2.

Compound		Weight% of elements				
		C	H	N	Cu	O
Cu_3BTC_2	calc.	35.74	1.00	0	31.52	31.74
	found	35.45	1.03	0.00	31.1	
0.1 TCNQ@Cu_3BTC_2	calc.	36.88	1.03	0.90	30.49	30.70
	found	35.82	1.01	1.17	28.6	
0.2 TCNQ@Cu_3BTC_2	calc.	37.95	1.06	1.74	29.52	29.73
	found	36.98	1.09	2.21	28.0	
0.3 TCNQ@Cu_3BTC_2	calc.	38.95	1.09	2.52	28.62	28.82
	found	38.11	1.12	2.81	27.3	
0.4 TCNQ@Cu_3BTC_2	calc.	39.89	1.12	3.26	27.77	27.96
	found	39.13	1.13	3.71	25.9	
0.5 TCNQ@Cu_3BTC_2	calc.	40.77	1.14	3.96	26.97	27.16
	found	39.87	1.15	4.52	24.8	
0.6 TCNQ@Cu_3BTC_2	calc.	41.61	1.16	4.62	26.21	26.39
	found	41.42	1.19	5.23	24.3	
0.7 TCNQ@Cu_3BTC_2	calc.	42.40	1.19	5.24	25.94	25.67
	found	42.10	1.28	5.72	24.2	
0.8 TCNQ@Cu_3BTC_2	calc.	43.15	1.21	5.83	24.82	24.99
	found	43.27	1.27	6.84	22.5	
0.9 TCNQ@Cu_3BTC_2	calc.	43.86	1.23	6.39	24.17	24.34
	found	43.61	1.21	6.97	22.5	
1.0 TCNQ@Cu_3BTC_2	calc.	44.54	1.25	6.92	23.56	23.73
	found	45.12	1.38	8.08	21.2	

Liquid phase infiltration

Pristine, activated Cu_3BTC_2 (150 mg) was immersed in a saturated TCNQ solution in DCM (100mL) and stirred for 5 days. The resulting green powder was collected via filtration and dried in ambient air.

The PXRD pattern (Figure S 21) of TCNQ@Cu_3BTC_2 shows that the overall crystal structure of the MOF is retained and no new reflections appear, as was seen for material synthesized via the vapor phase. Moreover, the (111) reflection is not pronounced suggesting that the TCNQ molecules are not preferentially accommodated in the (111) lattice plane due to the presence of solvent molecules in the pores. Elemental analysis (Table S 3) reveals overall lower weight percentages due to the adsorption of water in the pores and a C/N ratio that matches with a loading of x = 0.4 TCNQ molecules per formula unit Cu_3BTC_2. SEM images (Figure S 22) show octahedral MOF crystallites surrounded by further smaller fragments and no indication for the formation of CuTCNQ. EDX mapping (Figure S 23) shows a homogenous element distribution indicating that the material around the octahedra are fragments of the MOF crystallites that have formed due to the mechanical stress while stirring. *IV* curves of a pressed pellet of the material show a conductivity in the order of 10^{-4} $S \cdot cm^{-1}$. This is higher than for material with equivalent loading synthesized via the vapor phase which is likely due to different particle sizes and the

presence of additional solvent and water molecules inside the pores, which causes a non-linear (non-ohmic) behavior of the *IV* curve.

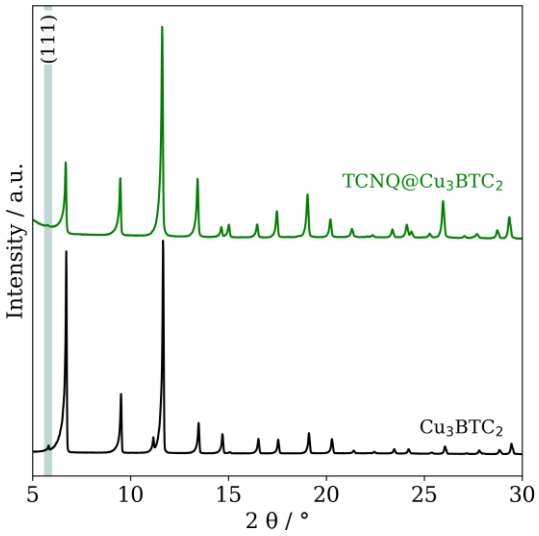

Figure S 21: PXRD of pristine Cu_3BTC_2 (black) and TCNQ@Cu_3BTC_2 synthesized via liquid phase infiltration (green).

Table S 3: Elemental analysis of the concentration series of TCNQ@Cu_3BTC_2.

Compound	Weight% of elements			
	C	H	N	Cu
0.4TCNQ@Cu_3BTC_2 + n H_2O	27.42	3.98	2.20	18.3

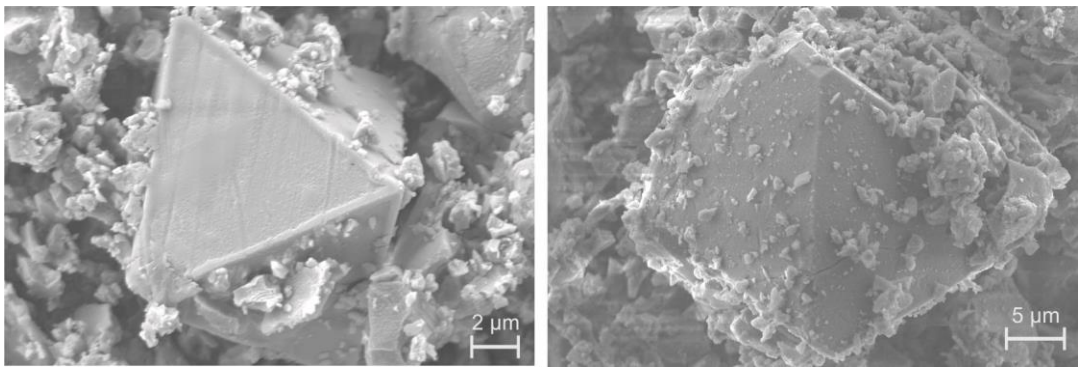

Figure S 22: SEM images of TCNQ@Cu_3BTC_2 synthesized via liquid phase infiltration.

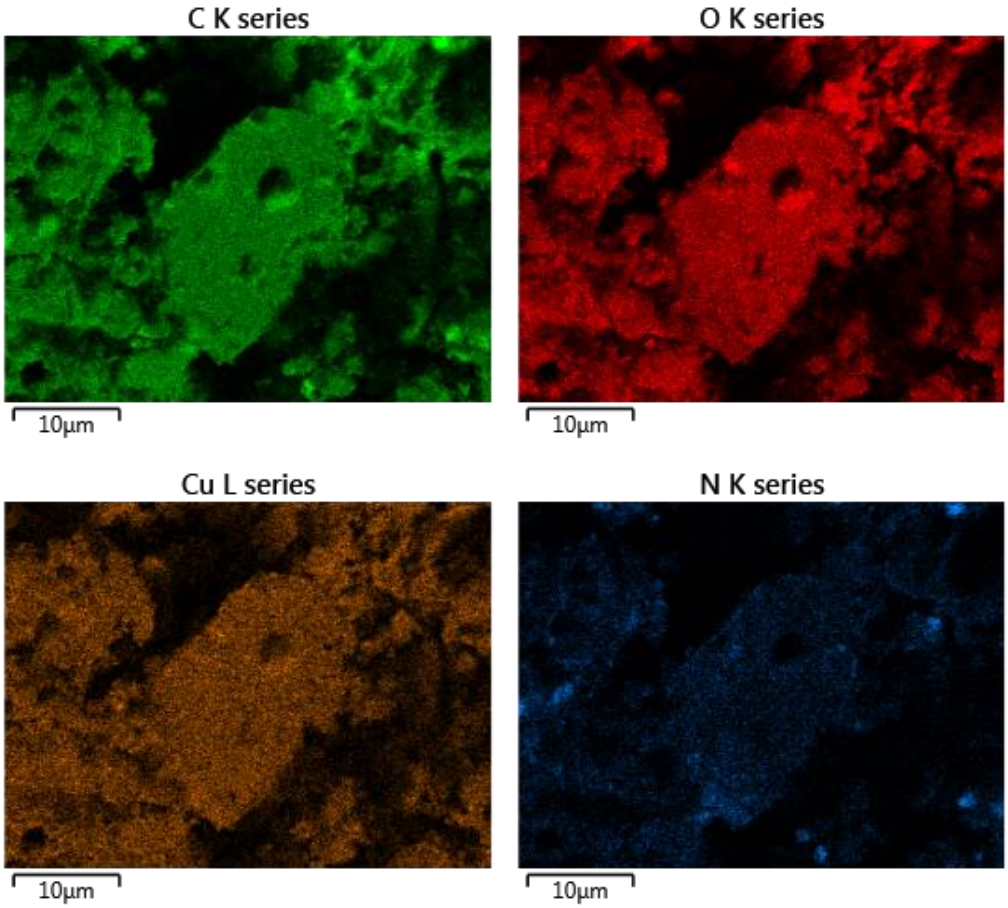

Figure S 23: EDX elemental mapping of TCNQ@Cu_3BTC_2 synthesized via liquid phase infiltration.

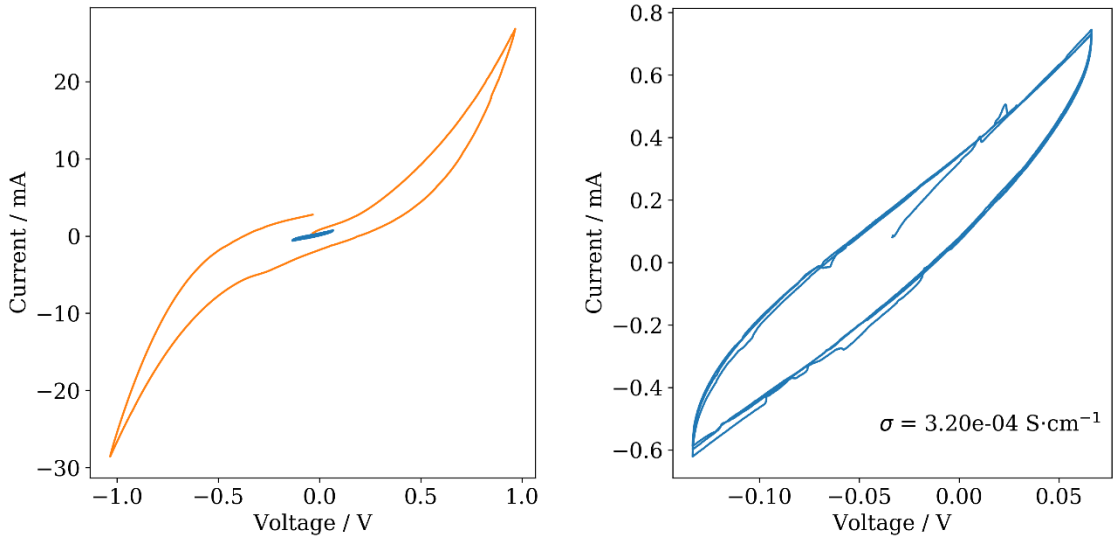

Figure S 24: *IV* curves of TCNQ@Cu_3BTC_2 synthesized via liquid phase infiltration. Orange curve shows non-ohmic behavior at potentials of ±1 V. Measurement at low potentials (blue) was used to calculate the conductivity of the material. Pellet thickness is 0.44 mm.

References

[1] R. A. Heintz, H. Zhao, X. Ouyang, G. Grandinetti, J. Cowen, K. R. Dunbar, *Inorg. Chem.* **1999**, *38*, 144-156.

[2] N. Nijem, H. Bluhm, M. L. Ng, M. Kunz, S. R. Leone, M. K. Gilles, *Chem. Commun.* **2014**, *50*, 10144-10147.

[3] J. Szanyi, M. Daturi, G. Clet, D. R. Baer, C. H. F. Peden, *Phys Chem Chem Phys* **2012**, *14*, 4383-4390.

[4] M. J. Capitán, J. Álvarez, C. Navio, *Phys Chem Chem Phys* **2018**, *20*, 10450-10459.